# Mechanical modulation of docetaxel-treated bladder cancer cells by various changes in cytoskeletal structures

Joanna Zemla, Claude Verdier, Marcin Luty, Joanna Pabijan, Malgorzata Lekka

# Mechanical modulation of docetaxel-treated bladder cancer cells by various changes in cytoskeletal structures

Joanna Zemła[1*], Claude Verdier[2], Marcin Luty[1], Joanna Pabijan[1], Małgorzata Lekka[1]

[1] Institute of Nuclear Physics Polish Academy of Sciences, PL-31342 Krakow, Poland

[2] Univ. Grenoble Alpes, CNRS, LIPhy, F-38000 Grenoble, France

[*]Corresponding author: joanna.zemla@ifj.edu.pl

## Abstract

Cytoskeleton targeting agents are a group of chemotherapeutics used in the therapy of many types of cancer, such as breast, prostate, lung, bladder cancer, and others. At the same time, the assessment of the rheological properties of cancer cells is a relevant marker of their metastatic potential and therapeutic efficacy. For these reasons, understanding the interaction between the actin microfilament (MFs) network, microtubules (MTs), and so-called intermediate filaments (IFs) is crucial for the use of the rheological properties of cells as biomechanical markers. The current work compares the rheological properties of bladder cancer cells T24 and 5637, which differ in cytoskeletal composition, treated with a low dose of docetaxel (DTX) - a microtubule targeting agent (MTA). AFM revealed that 5637 cells stiffen over time when exposed to DTX, whereas changes in rheological properties of T24 cells are less pronounced, and both softening and stiffening of cells are observed. From immunostaining and Western blot analysis, we found that in addition to changes in the content and organization of MTs, reorganization of MFs and vimentin IFs also occurs. We show that both cell and nucleus morphology changes after DTX treatment. DTX treatment decreases and increases the migratory potential of 5637 and T24 cells, respectively. The current work shows that vimentin IFs modulate the mechanosensitivity of bladder cancer cells.

## Graphical abstract

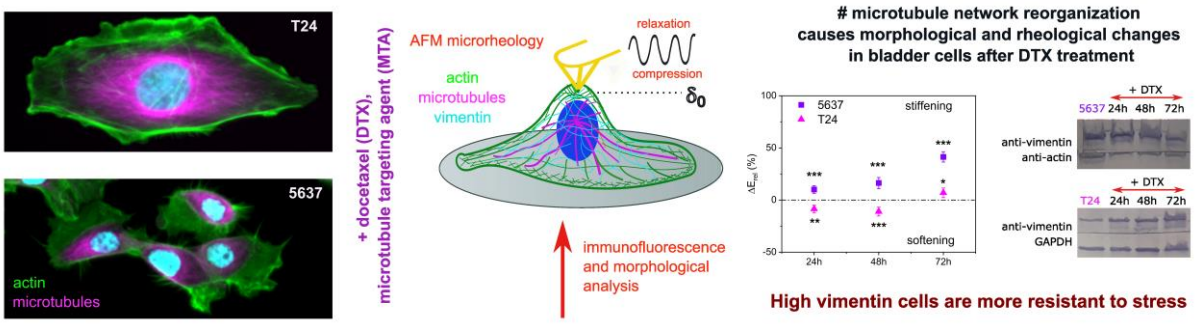


**Keywords**: AFM micro-rheology, cell viscoelasticity, cell cytoskeleton, chemotherapeutics, power-law rheology

## 1. Introduction

Over two decades since atomic force microscopy (AFM) was introduced to measure the mechanical properties of individual cells, both cancerous and normal (Lekka et al., 1999a). During this time, AFM systems have been modified to study the elastic and viscoelastic properties of cells. Studies of the bladder (Abidine et al., 2018; Ramos et al., 2014), brain, breast, lung, skin cells (Bobrowska et al., 2016; Hosseini et al., 2022, 2021), and many others revealed that cancer cells are more deformable than normal cells. It was concluded that the mechanical properties studied by AFM depend on the organization of the actin network, one of the three main components of the cell cytoskeleton. Besides the actin microfilaments (MFs) network, other biopolymers that participate in maintaining cell shape are microtubules (MTs) and so-called intermediate filaments (IFs). The most abundant is vimentin, which is found predominantly in cells of mesenchymal origin (Kraxner et al., 2021). In addition to maintaining cell shape, actin, microtubule, and vimentin networks play other roles in optimal cellular functioning. It is known that the MFs, MTs, and vimentin intermediate filaments (VIFs) interpenetrate and that reorganization of one of them can induce structural changes in the other two biopolymer networks, causing a cascade of severe consequences for the legitimate functioning of cells.

In recent years, a substantial interest has appeared in microtubule-targeting agents (MTAs) for cancer treatment. Among these, taxanes have been used in the therapy of various cancers such as ovarian, breast, and uterine, but also head and neck cancers, non-small lung cancer, prostate, and bladder since the 1990s (Čermák et al., 2020; Fojo and Menefee, 2007; Kubiak et al., 2021;

Škubník et al., 2021). Taxanes are microtubule targeting agents (MTs depolymerization is inhibited and an increase in microtubular mass occurs), which, at low concentrations, block the cell cycle in mitosis and usually induce caspase-dependent apoptosis (Michalakis et al., 2005; Morse et al., 2005; Smith and Xu, 2021). MTAs have been used to gain more insight into the role of microtubules in cell mechanics. By MT stabilization, one would expect stiffening of cells treated with MTAs; however, research data are inconsistent (Kubiak et al., 2020). Some reports show an increase in the apparent Young's modulus denoting cell stiffening, while others demonstrate that cells soften after paclitaxel (PTX) or docetaxel (DTX) treatments. For example, in 2011, Derely et al. (Derely et al., 2011) showed with combined Raman confocal microscopy and AFM studies in MCF-7 epithelial breast cancer cells that PTX acts on microtubules, but its molecules also accumulate around the nucleus and in the cell membrane (Derely et al., 2011). They also reported softening of PTX-treated MCF-7 cells. Kaffas et al. proved that the complex shear modulus increases in PTX-treated MCF-7 cells, as measured by particle tracking microrheology (El Kaffas et al., 2013). In their study, lower PTX doses and longer exposure times were used, demonstrating that the dose and time of exposure to the agent are critical. The influence of taxanes on the mechanical properties of human leukemic monocyte lymphoma (U937 cells), pancreatic (PC-3), ovarian adenocarcinoma (SKOV-3 cells), and prostate (DU145 cells) cancer has been investigated recently (Hou et al., 2021; Hung and Tsai, 2015; Kubiak et al., 2021, 2020; Ren et al., 2015). In the case of U937, SKOV-3, and PC-3 cells, cell stiffening was observed and concluded to be an expected effect as taxanes induce MT polymerization. However, studies by Kubiak et al. (Kubiak et al., 2021) showed that in the case of prostate cancer cells treated with DTX, the cell stiffening resulted from the crosstalk between the actin filament and microtubule networks. The increased resistance of DU145 cells to compression after DTX treatment was accompanied by the reorganization of the MTs network around the nuclei and by the markedly increasing amount of actin fibers at the periphery of DTX-treated cells. These studies showed that perturbations induced in one of the cytoskeletal components induce changes in the other components, demonstrating that the complex structure and function of the cell cytoskeleton are not yet fully understood.

In this study, we investigated the effect of the low dose of DTX on the microrheological properties of bladder cancer (BC) cells and the structural changes in the cytoskeleton, focusing on the involvement of different cytoskeletal components in the mechanical stability of cells. BC is the ninth most commonly diagnosed cancer worldwide. It is associated with significant morbidity, mortality, and costs (Antoni et al., 2017; Sanli et al., 2017). Therefore, new

approaches to BC treatment are being introduced. Recently, clinical trials on applying gemcitabine and docetaxel treatment for BC are underway (Patel et al., 2023; Roumiguié and Black, 2022). This is another factor motivating for comprehensive studies of the interaction of bladder cancer cells and DTX. We used microscopic techniques, AFM-based microrheology, epi-fluorescence and confocal microscopy, and biological analytical methods (Western blot and cell viability assays) to address this issue. We chose two bladder cancer cell lines, 5637 and T24, whose cytoskeletons are formed by MTs, MFs, and VIFs, differ significantly in their actin content. In 5637 cells, the amount of actin is very low, whereas the cytoskeleton of T24 cells is rich in actin filaments. These two cell lines also show significantly distinct invasive potential. T24 cells migrate much faster than 5637 cells (Luty et al., 2023;). In parallel, as shown by Tang et al. (Tang et al., 2023), a large amount of T24 cells (~1200 cells) transmigrated through a Matrigel with a pore size of 8 μm toward 5% serum, while for the 5637 cell line, less than 100 cells passed through such a barrier.

In our research, we showed that low-dose DTX treatment, directly and indirectly, induces changes in the organization and concentration of all major cytoskeletal components in T24 cells, preserving their microrheological properties. It is not the case for 5637 cells, where we observed DTX-induced cell stiffening and no compensatory effects in actin or vimentin networks, suggesting that compensation by one component for other cytoskeletal components induced changes is cell-type dependent.

## 2. Materials and Methods

### 2.1. Cell cultures

Two bladder cell lines with epithelial origin have been studied: urinary bladder cell carcinoma (5637, grade II, ATCC, LGC Standards) and transitional cell carcinoma (T24, ATCC, LGC Standards). Both cell lines were cultured in RPMI-1640 medium (Sigma) supplemented with 10% Fetal Bovine Serum (FBS, Sigma). The cells were cultured on plastic Petri dishes (TPP) at 37 °C in a 95% air/ 5% $CO_2$ atmosphere. 24h after seeding, the cell culture medium was supplemented with docetaxel (DTX, Merck), and the drug concentration was 0.5 nM. The cells were measured 24, 48, and 72 hours after DTX addition. The AFM measurements were performed at room temperature in the RPMI-1640 medium.

### 2.2. AFM-based force spectroscopy

A Nanowizard 4 AFM (JPK, Germany) was used to examine the nanomechanical properties of DTX-treated cells. The AFM is combined with an inverted optical microscope (IX71, Olympus, Japan) to control sample-probe localization. The cells were probed with soft (nominal spring constant of 0.01 N/m) triangle MLCT-C cantilevers (Bruker, Germany) with a four-sided pyramidal tip. The probes were calibrated using the thermal noise method (Sader et al., 1999; Schillers et al., 2017). Each cell was examined over the nuclear region, and the scanning area was 4 µm × 4 µm, over which a 16-pixel grid was collected.

The nanomechanical properties of cells were quantified using the apparent Young's modulus ($E$) calculated as a function of indentation ($\delta$). The probing depth was obtained by subtracting the calibration curve recorded on a non-deformable surface. To determine a contact point, the baseline is overlaid with a horizontal line, the decoupling of which tells the contact point used for $\delta$ calculation (Ramos et al., 2014; Zemła et al., 2020). The obtained force curves were fitted with Sneddon's modification of the Hertz model (Lekka et al., 1999; Schillers et al., 2017), assuming that a cone can approximate the four-sided pyramid of the probing tip. The relation between the loading force ($F$) and the indentation is:

$$F(\delta) = \frac{2E_{sample}\tan(\alpha)}{\pi(1-\mu_{sample}^2)}\delta^2, \quad (1)$$

which is true when Young's modulus of the probe is several orders of magnitude larger than $E_{\text{sample}}$. $\mu_{sample}$ is the Poisson's ratio, which relates to the compressibility of the sample. It has been set to 0.5, as cells are assumed to be incompressible. α is a half-open angle of the probe, and for MLCT, it is 21 degrees. Data were normalized to control samples according to the following equation:

$$\Delta E = \left(\frac{E_{DTX}-E_{ctr}}{E_{ctr}}\right) * 100\%. \quad (2)$$

$E_{DTX}$ and $E_{ctr}$ are apparent Young's moduli of cells non-exposed or exposed to DTX, respectively, and they are expressed as mean ± standard error of the mean (SEM).

### 2.3. AFM-based microrheology

The experiments were performed with a Nanowizard II AFM (JPK, Germany), accessible in the Laboratory of Interdisciplinary Physics (LIPhy) at University Grenoble Alpes, operating in force modulation mode. We applied MLCT-C cantilevers, calibrated using the thermal noise method (Sader et al., 1999; Schillers et al., 2017). Measurements were conducted for six modulation frequencies ranging from 1 to 300 Hz. One modulation cycle was recorded within

the nuclear region on one cell. A minimum of 50 cells was measured. The AFM head is mounted on an inverted fluorescence microscope (Observer D1, Zeiss, Germany).

### 2.3.1. Oscillations using an AFM

In microrheological mode, a cell is indented with an AFM probe at a certain depth ($\delta_o$), and then small sinusoidal deformations ($\delta$) at a given frequency ($f$) are superimposed. The initial indentation was below 1 μm to avoid distorting the results stemming from the substrate stiffness. Cantilever displacement is registered with a photodiode, and therefore, the force is derived analogously as in classical force spectroscopy (i.e., by multiplying cantilever deflection by the cantilever spring constant). The relation between the force and the indentation for a conical probe is given by:

$$F_0 = \frac{3E_{sample}\tan\alpha}{4\,(1-\mu^2)}\delta_0^2. \quad (3)$$

Thus, we impose the piezo displacement Z and therefore, the indentation $\delta(\omega)$ and the force response $F(\omega)$ is measured, as previously described (Abidine et al., 2021, 2018, 2015). We assume that $\delta << \delta_o$ and account for the relationship between complex shear modulus ($G^*$) and the apparent Young's modulus, i.e., $G^* = E^*/(2*(1+\mu))$. After linearization, the final relationship is obtained:

$$G^*(\omega) = G' + iG'' = \frac{1-\mu}{3\,tan\alpha\,\delta_0}\left(\frac{F^*(\omega)}{\delta^*(\omega)} - i\omega b(0)\right). \quad (4)$$

where $G'$ and $G''$ are storage and loss moduli, characterizing elastic and viscous properties of the sample, respectively. The $i\omega b(0)$ part of the formula is an amendment regarding the hydrodynamic drag created by oscillations of the cantilever in the fluid. The drag depends on the viscosity of the medium, velocity, and tip geometry. It was found that $b(0) = 6.95 \cdot 10^{-6}$ Ns/m for the MLCT-C cantilevers (Abidine et al., 2021).

### 2.3.2. Rheological model

The most common approach is to model viscoelastic data with a power law, i.e., $G'$ and $G''$ change with a power of the frequency ($f$), $G \sim f^{\beta}$ in a given frequency range (Abidine et al., 2021; Alcaraz et al., 2003; Flormann et al., 2021; Hecht et al., 2015). The power $\beta$ is a dimensionless number characterizing the degree of dissipation of such a material. For a purely elastic solid, $\beta = 0$ (using $G'$), while for an ideal viscous Newtonian fluid, $\beta = 1$ (using $G''$). Typically, the power-law exponent of living cells varies from 0.1 to 0.3 (Abidine et al., 2021; Alcaraz et al., 2003). However, a single-power law exponent rarely covers the whole frequency range, thus, a

double-power law behavior, proposed by Abidine et al. (Abidine et al., 2021), is applied here. Storage and loss moduli frequency dependence is of the following form:

$$G' = G_0(\frac{f}{f_0})^a + G_1(\frac{f}{f_0})^b, G'' = G_2(\frac{f}{f_0})^c + G_3(\frac{f}{f_0})^d, \quad (5)$$

and $f$ is expressed in Hz, and $f_0$ = 1Hz. As a result, we get prefactors $G_0$, $G_1$, $G_2$, $G_3$ expressed in Pascals (Pa), while exponents $a, b, c, d$ are dimensionless. When a plateau for $G'$ is obtained at low frequencies $a$ = 0, and $G_0$ is the elastic plateau modulus. We note further that for low frequencies when the second term is negligible, $G' \sim G_0(f/f_0)^a$ so $G_0 \sim G'(1Hz)$, and similarly $G'' \sim G_2(f/f_0)^c$ so $G_2 \sim G''(1Hz)$. The transition frequency $f_T$ corresponded to $G'(f_T) = G''(f_T)$ and was calculated by iterations of the following equation:

$$G_0(\frac{f}{f_0})^a = G_2(\frac{f}{f_0})^c + G_3(\frac{f}{f_0})^d, \quad (6)$$

after neglecting the second term in G'.

Fitting parameters ($G_0$, $G_2$, and transition frequency $f_T$) are normalized w.r.t. the apparent shear Young's moduli (see eq. 2).

### 2.4. Immunostaining of actin filaments and microtubules

Control and DTX-treated cells (24 h, 48 h, and 72 h) at a density of 30,000 cells per well were cultured in 24-well plates (TPP). Before staining, the cell culture medium was removed, and the cells were rinsed with phosphate-buffered saline (PBS, Sigma-Aldrich). Cells were then fixed in 3.7% paraformaldehyde (20 minutes at room temperature) and washed with PBS, cold 0.2% Triton X-100 solution, and PBS again. The cells were then incubated with Alexa Fluor 488-conjugated phalloidin (Molecular Probes, Thermo Fisher Scientific, Waltham, MA, USA) diluted at 1:200 in PBS for 30 minutes and then incubated overnight with anti-β-tubulin antibody conjugated with the fluorescent dye Cy3 (Sigma-Aldrich, Poznań, Poland), also diluted at 1:200 in PBS. Finally, nuclei were stained with Hoechst 33342 dye (Sigma-Aldrich, Poznań, Poland) at a dilution of 1:200 in PBS. After each staining step, the samples were rinsed three times with PBS.

### 2.5. Cell imaging with epi-fluorescent and confocal microscopy

Confocal images of actin and tubulin networks were performed with a confocal microscope accessible in the Laboratory of *in vivo* and *in vitro* imaging at Maj Institute of Pharmacology, Polish Academy of Sciences. The Leica TCS SP8 WLL confocal microscope, equipped with

new-generation HyD detectors set at 405-500 nm (Hoechst) and 509-560 nm (Alexa Fluor 488) was used. Fluorescent dyes were excited by diode lasers: 405 nm (Hoechst) and white light laser with emission wavelength set at 499 nm (AlexaFluor 488). Images were registered using an oil immersion 63x objective lens (HC PL APO CS2 NA 1.40)

Epi-fluorescence images were acquired using an inverted fluorescence microscope (Olympus IX83) equipped with an objective LUCPlanFLN (20x), 100 W mercury lamp, and a set of filters with maximum emission at 594 nm and 420 nm. Images were recorded with an XC10 camera (1.4 million pixels).

### 2.6. Determination of the cell projected area

The single-cell projected area was calculated using a macro supported in ImageJ software (open source code, https://imagej.net/software/fiji/), developed by Prauzner-Bechcicki et al. (Prauzner-Bechcicki et al., 2015). For each image, the number of nuclei and the projected cell spreading area of all cells ($S_{total}$) were calculated. Then, $S_{total}$ was divided by the number of nuclei, and the single-cell projected area ($S$) was obtained. The single-cell projected area values are expressed as mean ± standard error of the mean (SEM) and are used to calculate relative cell projected areas ($\Delta S_{rel}$, according to a formula similar to eq. 2), i.e., changes concerning untreated cells.

### 2.7. Nuclear morphometric analysis

Filippi-Chiella et al. introduced an ImageJ plugin (Filippi-Chiela et al., 2012) that distinguishes normal and deformed nuclei in cells in 2D cultures. Nuclei of adhered cells vary in size but have a very regular shape. Thus, the analysis of the nuclei morphology of cells treated with several types of chemicals changing nuclei shape led to the suggestion of seven categories of nuclei. The distinction between the groups, normal (*N*), irregular (*I*), large regular (*LR*), large irregular (*LI*), small regular (*SR*), small (*S*), and small irregular (*SI*), is based on size and so-called nuclear irregularity index (*NII*), which is calculated from the aspect, area box, radius ratio and roundness of a nucleus. The critical step sets the threshold separating populations with normal and irregular nuclei.

### 2.8. Determination of cell height

The cell height was manually estimated during the AFM-based microrheological measurements. The AFM probe was brought into contact with the substrate next to the measured cell. The probe was then retracted from the surface (a few micrometers) and placed

over the measured cell using micrometric screws. The tip was then brought into contact with a cell surface using an approach command. Changes in the Z stage position were used to calculate the cell height.

### 2.9. Western blot

The Western blot (WB) method analyzed vimentin and tubulin expression levels in bladder cancer cells. Briefly, supernatants were separated on 10% SDS-PAGE gels and transferred to a polyvinylidene difluoride membrane. Vimentin (D21H3) XP® rabbit mAb (#5741) and mouse anti-α-tubulin monoclonal antibody were purchased from Cell Signaling Technology (Boston, USA) and Merck (Poznań, Poland), respectively. The aqueous solutions containing antibodies were used in the 1:1,000 ratio. Bands were visualized with horseradish peroxidase-conjugated anti-rabbit secondary antibody (Cell Signaling Technology). WB was performed in duplicate and repeated two times for each condition (n=4). The intensity of the WB bands was analysed using ImageJ software. Data are presented as mean ± SD. Statistical significance was tested by t-test (* $p<0.05$; ** $p<0.01$; *** $p<0.001$).

### 2.10. Migration assay

Cells were cultured as described in Section 2.1. 12-well plates (TPP) were used for the experiment. After a certain DTX incubation time, the plate was placed in the incubator chamber of the Olympus IX53 microscope, in which temperature, humidity, and $CO_2$ levels were controlled. Time-lapse monitoring of cell movement was carried out as described by Korohoda and Madeja (Korohoda and Madeja, 1997). Images of cells were taken 10 minutes apart over an 8-hour and 4-hour period in the case of control and DTX-treated samples, respectively. The analysis of the obtained images was carried out with the use of the Hiro software 1.0.0.4 (developed for the Department of WBBiB of the Jagiellonian University by Wojciech Czapla); this program analyzes the changes in the position of the cell centroid. Cell tracks are presented in circular diagrams in which the starting points of the trajectories are reduced to a common origin located at the center of the coordinate system. 50 cells were analyzed per case.

### 2.11. Assessment of DTX cytotoxicity by MTS assay

DTX cytotoxicity was obtained using an MTS assay (Sigma-Aldrich). T24 and 5637 cells were seeded in 24-well plates at 80,000 cells per well. The number of HCV 29 cells in a well was 40,000. After 24h in culture, the medium containing 10% FBS was replaced with 1 mL of RPMI-1640 supplemented with 1% FBS and different concentrations of docetaxel. DTX

concentrations were 0.1; 0.25; 0.5; 1.5; 3.0; 5.0; and 10nM. DTX incubation time was 24, 48, and 72h. After incubation with DTX, the drug-containing medium was replaced with 0.5 mL of RPMI-1640 (1% FBS). Next, 100 µL of CellTiter96®Aqueous One Solution Reagent was added to each well, and a plate was placed in the incubator for 2h. After the incubation, from each well, a volume of 100 µL was transferred to a 96-well plate (TPP), and absorbance at 490 nm was measured using a spectrophotometer (ELISA SPECTROstar Nano, BMG LABTECH). The experiment was repeated three times.

### 2.12. Statistical analysis

MTS data are presented as mean ± standard error of the mean (SEM). Data describing morphometric and cell motility properties of cells are expressed similarly. Original Young's modulus values were also calculated as mean ± SEM. Normalized values of cell area ($\Delta S_{rel}$), elastic plateau modulus $\Delta G_0^{rel}$, transition frequency ($\Delta f_T^{rel}$), and height ($\Delta h_{rel}$) were calculated according to a formula similar to eq. 2. Errors of normalized parameters were estimated from the error propagation method. The statistical significance of *E*, *S*, and *h* data was evaluated using Kruskal-Wallis ANOVA included in OriginPro 9.1 software. Cell migration speed and distance, also presented as mean ± SEM, were tested with the t-Student test at a 0.05 significance level. The following notation was applied: * $p < 0.05$; ** $p < 0.01$; *** $p < 0.001$. Migration data were also tested for significant outliers using Grubb's test. The number of cells measured and fluorescence images analyzed in this study are summarized in Table 1.

Table 1 Number of cells and fluorescence images used to obtain morphometric and microrheological parameters characterizing DTX-treated 5637 and T24 cells.

| ***measurement*** | **Cell line** | **# cells** | | | | | |
|---|---|---|---|---|---|---|---|
| | | Ctr 24h | DTX 24h | Ctr 48h | DTX 48h | Ctr 72h | DTX 72h |
| *Young's modulus* | 5637 | 87 | 82 | 25 | 48 | 105 | 113 |
| | T24 | 63 | 72 | 77 | 42 | 59 | 96 |
| *Rheological properties and cell height* | 5637 | 42 | 39 | - | - | 31 | 37 |
| | T24 | 51 | 95 | - | - | 47 | 93 |
| *Cell morphology, NII analysis* | 5637 | 7 (images) | | | | | |
| | T24 | 7 (images) | | | | | |
| *Cell migration* | 5637 | 50 | | | | | |
| | T24 | 50 | | | | | |

## 3. Results

### 3.1. Viscoelastic characterization of bladder cancer cell lines treated with low dose docetaxel.

We investigated the local mechanical properties of bladder cells using AFM and obtained DTX time-dependent relative changes in the apparent Young's modulus values ($\Delta E_{rel}$). In the case of 5637 cells, an increase in $\Delta E_{rel}$ is observed with time (Fig. 1a).

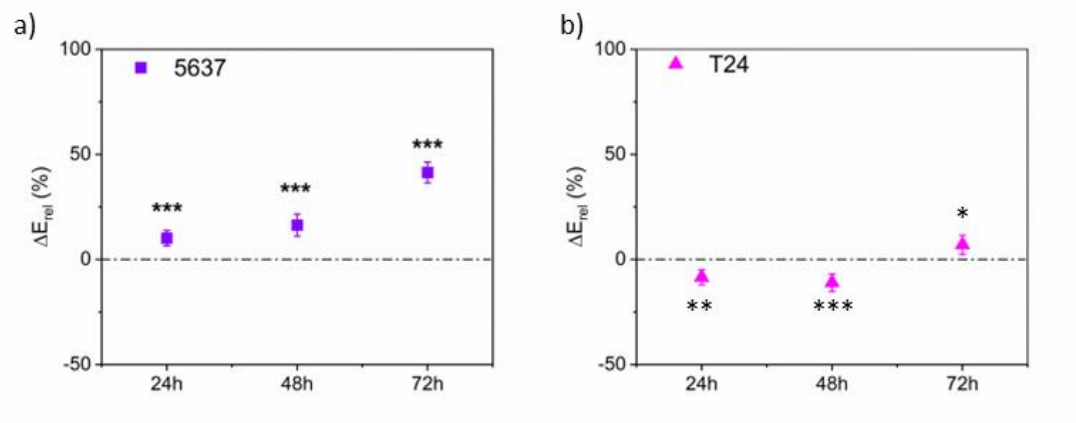


**Figure 1** The relative changes in the apparent Young's modulus (normalized to control) obtained for 5637 and T24 bladder cancer cells treated with DTX for 24h, 48h, and 72h. Statistical significance was tested with Kruskal-Wallis ANOVA (*$p < 0.05$; **$p < 0.01$; ***$p < 0.001$).

After 24 h of DTX treatment, $E_{DTX}$ is approximately 10% higher than Young's apparent modulus of control cells. Over time, the increase in $E_{DTX}$ becomes more pronounced, 16% at 48h and 41% at 72h. T24 cells respond differently (Fig. 1b), with $E_{DTX} < E_{ctr}$ at 24h and 48h decreasing by 8.5% and 11%, respectively. An opposite response to a drug stressor is observed after 72h when $E_{DTX} > E_{ctr}$ and the change is at the level of 7%.

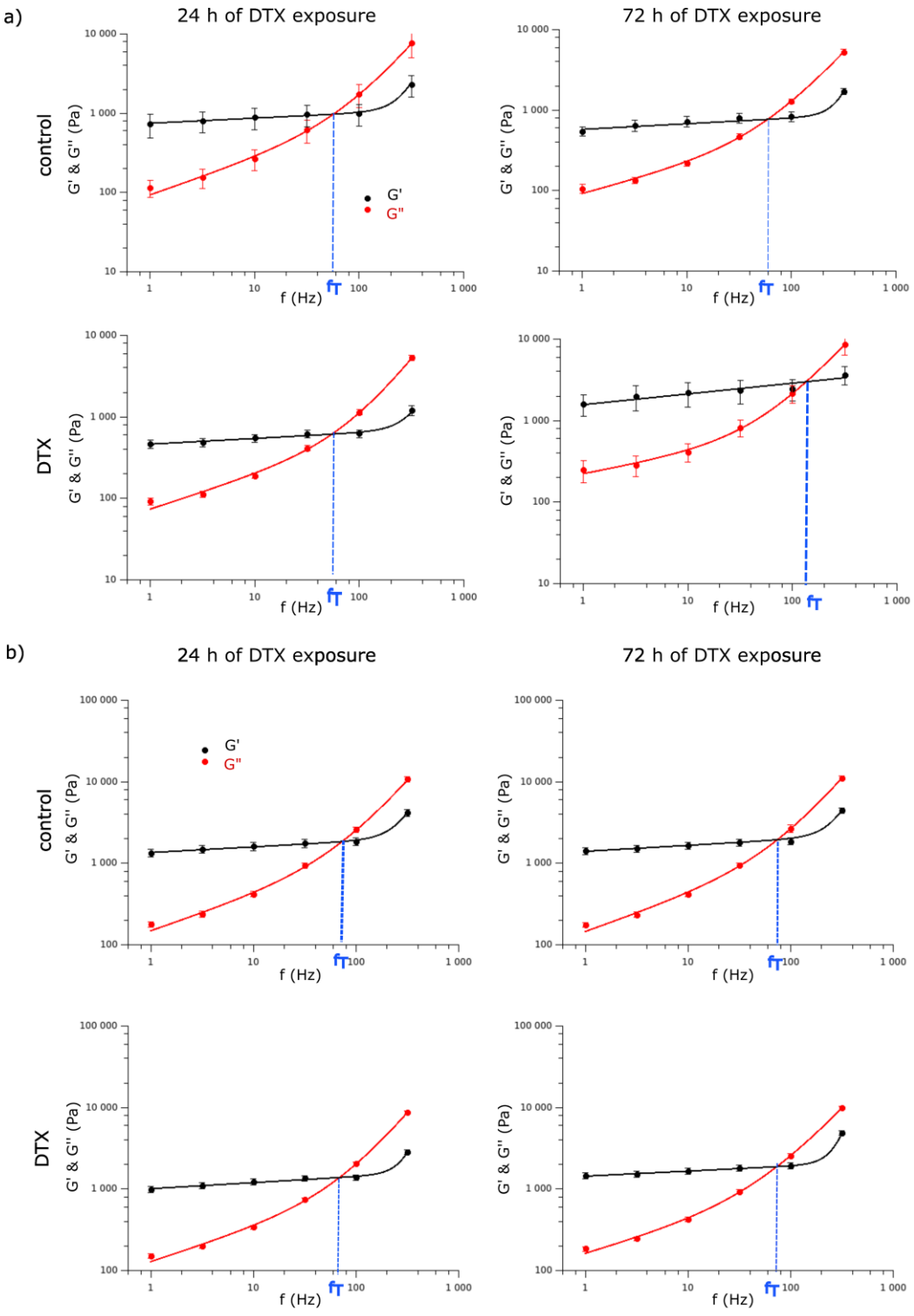


**Figure 2** Rheological properties of 5637 (a) and T24 (b) bladder cancer cells. Storage (*G'*, black) and loss (*G''*, red) moduli of cells treated with a low dose of DTX for 24h and 72h fitted with a double power law model. The transition frequency is indicated by vertical dash blue lines.

Next, we characterized the viscoelastic properties of the studied cells after 24 and 72 hours of low-dose DTX treatment. Figure 2 shows frequency-dependent changes in the viscoelastic properties of control and DTX-treated T24 and 5637 cells. In the low-frequency range, we observe typical solid-state viscoelastic behavior where $G' > G''$. In the high-frequency range, where $G' < G''$, the fluidization of the cells occurs. In the case of T24 and 5637 cells, $G'$ shows a weak power law dependence, with characteristic plateaus ($G_0$) at low frequencies (below 30 Hz). The shear elastic plateau module of 5637 cells is lower than $G_0$ of T24 cells (Table 2). For control cells (0 + 24h), it is 571 ± 31 Pa and 1363 ± 30 Pa, respectively. In both cases, there is no difference in the value of the exponent of the power law, being 0.086 ± 0.023 (5637 cells) and 0.07 ± 0.01 (T24 cells) for 48h in culture and 0.065 ± 0.016 (5637 cells) and 0.064 ± 0.010 (T24 cells) for 96h in culture.

DTX exposure alters the elastic response to oscillatory deformation of 5637 cells. After 72h of treatment, the shear elastic plateau modulus is 2~fold higher than for control cells. The power coefficient is also larger, 0.065 ± 0.016 vs 0.13 ± 0.03 for control and drug-exposed cells. For T24 cells, we observed a decrease in $G_0$ after 24h of DTX treatment compared to the control, while no difference in the shear elastic plateau modulus values was observed at 72h. Interestingly, no change in the power law exponent was observed regardless of the drug exposure time.

The viscous response of cells to frequency-dependent oscillatory deformations is described by the loss modulus, to which a double power-law model was fitted (Eq. 5). Examination of Table 2 and Figure 2 shows a strong power-law dependence of $G''$. At low frequencies, the loss modulus of 5637 cells varied strongly, which is emphasized by $G_2$ and $c$ parameters. After 24h of DTX treatment, we obtained a decrease in $G_2$, so less viscosity contribution to the overall mechanical properties of 5637 cells. In contrast, after 72h of DTX exposure, $G_2$ was greater ($\Delta G_2^{rel}$ = 2.38 ± 0.74), and the power coefficient $c$ decreased by about 50 % compared to the control (Table 2). In the case of T24 cells, we observed slight changes in $G_2$, but compared to control samples and after error propagation estimation, there is no pronounced change in $G''$ at low frequencies. Compared to the power ranges of the $G''$ function in the low and high-frequency ranges, $c$ changes from 0.24 to 0.45, and $d$ changes from 1.4 to 1.7, respectively. Both $G_3$ and $d$ are relevant to the transition frequency calculation.

**Table 2** Elastic plateau modulus ($G_0$), exponents of double power law models ($a$, $c$, $d$), $G_2$ and $G_3$ coefficients of G'', and transition frequencies ($f_T$) obtained from the fit of the double-power law model.

| ***parameter*** | **Cell line** | **Ctr 24h** | **DTX 24h** | **Ctr 72h** | **DTX 72h** |
|---|---|---|---|---|---|
| $G_0$ *(Pa)* | 5637 | 577 ± 31 | 463 ± 23 | 748 ± 28 | 1569 ± 169 |
| | T24 | 1363 ± 30 | 1010 ± 39 | 1402 ± 34 | 1439 ± 17 |
| *a* | 5637 | 0.086 ± 0.023 | 0.070 ± 0.020 | 0.065 ± 0.016 | 0.13 ± 0.03 |
| | T24 | 0.07 ± 0.01 | 0.074 ± 0.016 | 0.064 ± 0.010 | 0.062 ± 0.005 |
| $G_2$ *(Pa)* | 5637 | 91 ± 13 | 74 ± 14 | 93 ± 17 | 221 ± 29 |
| | T24 | 148 ± 23 | 128 ± 18 | 145 ± 24 | 160 ± 20 |
| *c* | 5637 | 0.35 ± 0.08 | 0.41 ± 0.09 | 0.45 ± 0.09 | 0.24 ± 0.08 |
| | T24 | 0.43 ± 0.08 | 0.41 ± 0.07 | 0.44 ± 0.08 | 0.37 ± 0.07 |
| $G_3$ *(Pa)* | 5637 | 0.96 ± 0.45 | 0.26 ± 0.19 | 0.59 ± 0.42 | 1.99 ± 0.87 |
| | T24 | 1.2 ± 0.74 | 0.82 ± 0.45 | 1.2 ± 0.8 | 2.7 ± 1.2 |
| *d* | 5637 | 1.47 ± 0.08 | 1.69 ± 0.12 | 1.61 ± 0.11 | 1.44 ± 0.08 |
| | T24 | 1.5 ± 0.1 | 1.58 ± 0.09 | 1.56 ± 0.1 | 1.40 ± 0.07 |
| $f_T$ *(Hz)* | 5637 | 64 | 55 | 57 | 132 |
| | T24 | 73 | 69 | 70 | 73 |

Figure 3 shows the changes in relative shear elastic plateau modulus (taken from the plateau) and relative transition frequencies of T24 and 5637 cells. These two parameters clearly distinguish the viscoelastic changes induced in the cells by DTX. In the case of T24 cells, a slight decrease in $G_0$ is observed after the 24h drug treatment, and a very small variation in $f_T$ (Fig. 3). On the contrary, the 5637 cells are characterized by the distinctive increases of both $G_0$ and $f_T$ ($\Delta G_0^{rel}$ = 1.10 ± 0.31 and $\Delta f_T^{rel}$ = 1.3) after 72h of culture in DTX-containing medium, which implies the stiffening of the 5637 cells and their increased resistance to the applied deformations, respectively.

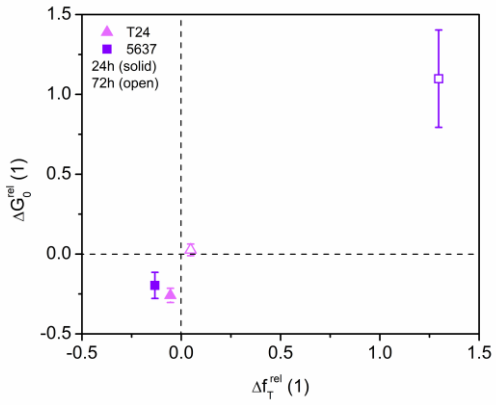


**Figure 3** Normalized shear elastic plateau modulus ($\Delta G_0^{rel}$) and transition frequency ($\Delta f_T^{rel}$) of T24 (triangles) and 5637 (squares) bladder cells treated with a low dose of DTX for 24 and 72 hours, solid and open data points, respectively.

### 3.2. Cell morphology after low-dose DTX treatment.

Exposure of bladder cancer cells to DTX caused their morphological changes depending on the exposure time. Significant changes in cell height and cell projected area were observed for T24 and 5637 cells after 24h of exposure to the drug (Fig. 4a). DTX treatment resulted in an approximately 23% increase in the height of T24 and 5637 cells (21.8% ± 6.8% and 22.8% ± 7.8%, respectively). The decrease in mean cell projected area of 33.4% ± 9.6% was observed for 5637 cells, while 24 hours of DTX exposure of T24 cells resulted in a decrease in cell projected area at the level of 25% (Fig. 4). After 72 hours of drug treatment, there were no significant differences in the height and cell projected area in the case of T24 cells. In contrast, the height of 5637 cells increased (19.4% ± 6.9%) while the mean projected cell area of DTX-treated cells did not differ from that of control 5637 cells ($\Delta S_{rel}$ = 14% ± 14%). Similarly, after 48 hours of DTX treatment, $\Delta S_{rel}$ of both T24 and 5637 cells was close to zero within the error bar (Fig. S2). While there is no clear correlation between $\Delta E_{rel}$ and $\Delta S_{rel}$ as a function of the DTX exposure time (Fig. 4c), the increase in height and elastic modulus of treated 5637 cells was preserved (Fig. 4b). In the case of T24, a slight increase in the height of treated cells was accompanied by a lower mean value of elastic modulus compared to control cells (Fig. 4b).

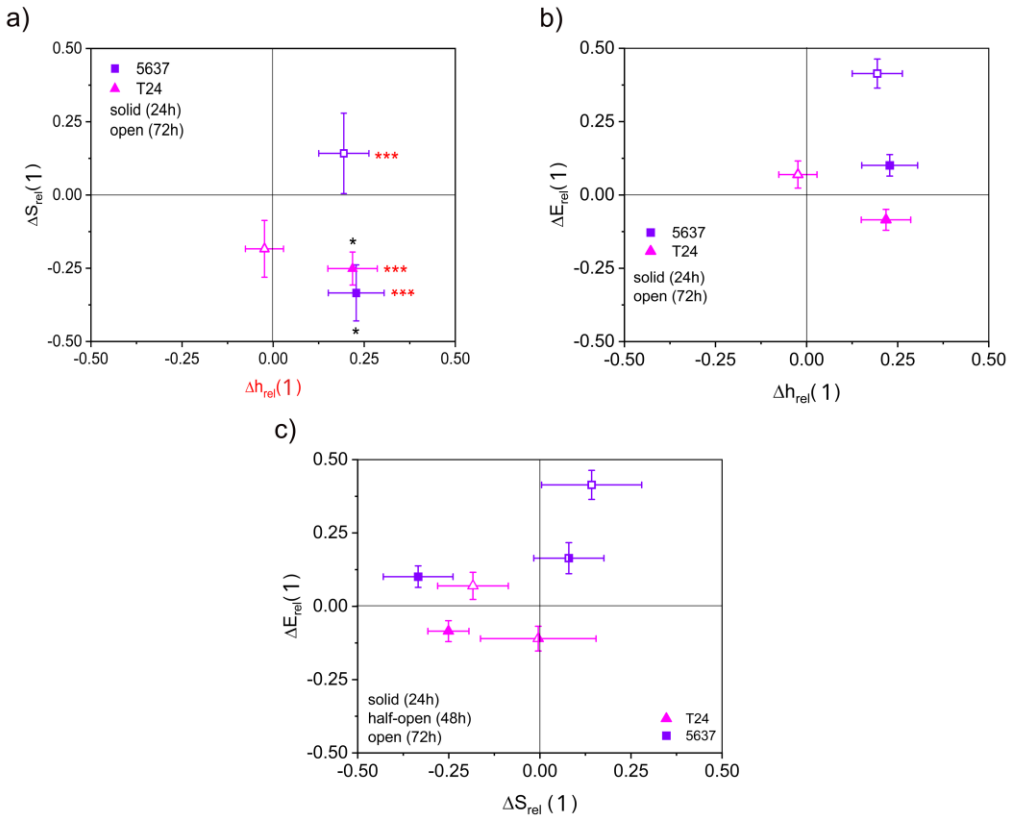


376

377 Figure 4 The relation between cell height and mechanical properties of T24 (triangles) and 5637
378 (squares) cells exposed to DTX. (a) Changes in cell height ($\Delta h_{rel}$) and cell projected area ($\Delta S_{rel}$)
379 after 24 and 72 hours of DTX treatment (solid and open symbols, respectively). (b) Variation
380 of the relative elastic modulus ($\Delta E_{rel}$) in relation to the relative cell height with respect to DTX
381 exposure time. (c) Variation of the $\Delta E_{rel}$ in relation to the $\Delta S_{rel}$ with respect to DTX exposure
382 time. Statistical significance was tested with Kruskal-Wallis ANOVA (* $p<0.05$; ** $p<0.01$;
383 *** $p<0.001$).

384 3.3. Cytoskeleton reorganization caused by DTX treatment.

385 Exposure to low-dose DTX induces changes in the organization of the cytoskeleton in both
386 studied bladder cell lines. Confocal microscopy images of actin fibers and microtubule
387 networks show that in 5637 cells, actin is localized at the cell edges, whereas in T24 cells, actin
388 filaments form stress fibers and are also abundant at the periphery of spreading T24 cells
389 (Fig. 5). Overall, actin is more abundant in T24 cells than in 5637 cells. Exposure to DTX
390 results in the reorganization of the actin, microtubule, and vimentin networks. Figure 5a shows
391 images of actin and MTs organization in 5637 cells exposed to docetaxel. The intensity of the
392 actin signal is lower after drug treatment.

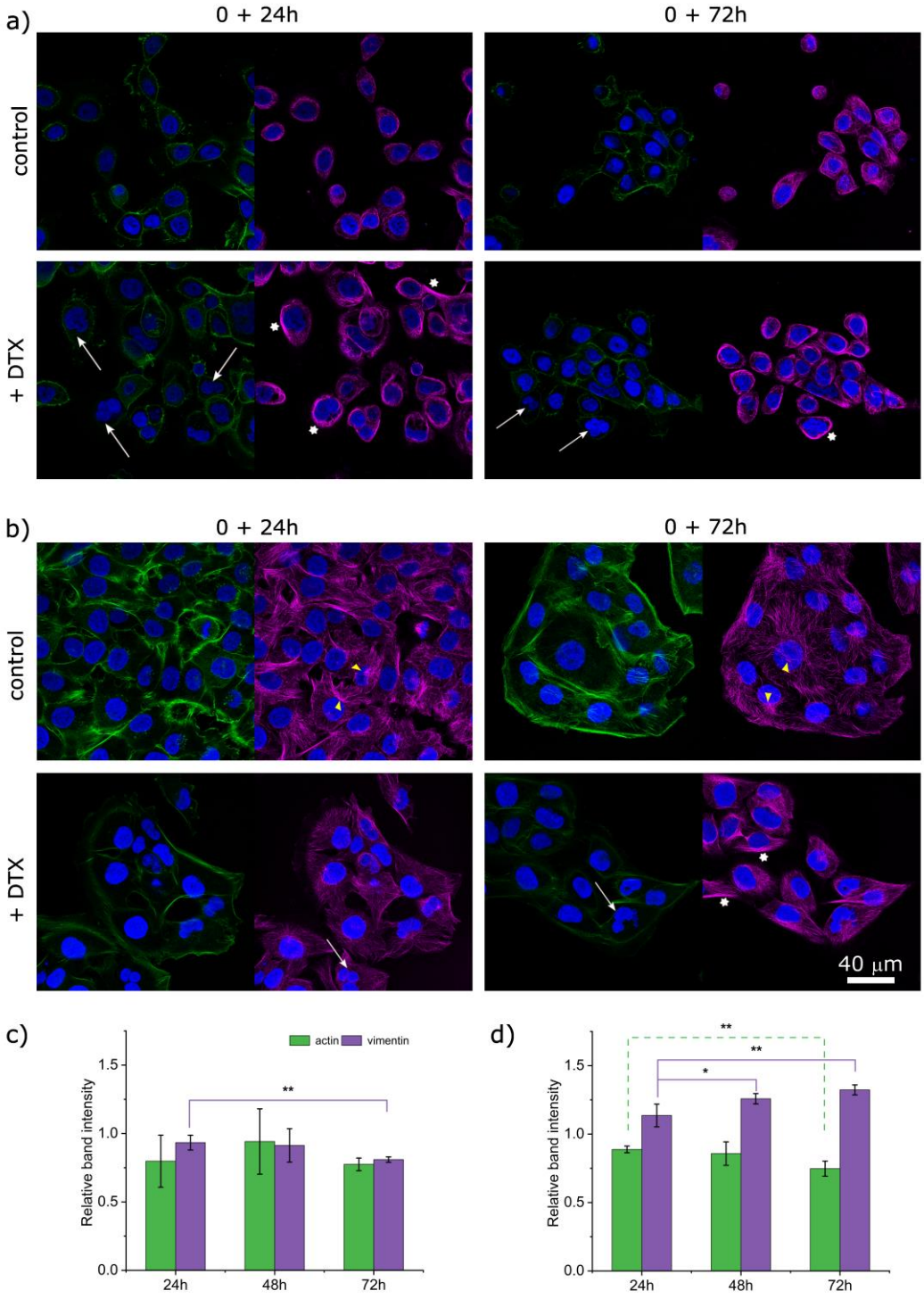


Figure 5 Cytoskeleton organization in 5637 (a) and T24 (b) cells before and after treatment with low-dose DTX. Actin and tubulin are green and magenta, respectively, and nuclei are blue. White arrows point to multinucleated cells, and white stars indicate tightly packed and concentrated microtubules. Microtubule organizing centers (MTOCs) are marked with yellow

arrowheads. The scale bar refers to all confocal images. Results of the Western blot showing changes in actin and vimentin content in 5637 and T24 cells, (c) and (d), respectively. Data normalized to the control and presented as means ± SD (n = 4). Statistical significance was tested with the t-test (* $p<0.05$; ** $p<0.01$; *** $p<0.001$).

In contrast, an increase in microtubule density is observed (Fig. 5a, marked with white stars), and MTs are tightly packed around the nucleus of the cell. In the case of T24 cells, 24 hours of DTX treatment causes actin aggregation at the regions adjacent to cellular protrusions. After 72h of the drug treatment, the actin signal appears to be much weaker (Fig. 5b). There are no noticeable changes in the microtubule network organization after 24h exposure of T24 cells to DTX. However, after 72h, we find an increased density of microtubules close to the nuclei, and the characteristic radial alignment of MTs is disturbed. While microtubule organizing centers (MTOCs) are easily detected in control T24 cells, MTOCs are difficult to locate in DTX-treated T24 cells (Fig. 5b, yellow arrowheads). In both cell lines, irregular nuclear shapes or multinucleated cells are observed after docetaxel treatment (Fig. 5, white arrows).

The vimentin and actin content in 5637 and T24 cells was examined by Western blot analysis. The longer 5637 cells were exposed to DTX, the less vimentin was detected (Fig. 5c). In contrast, exposure of T24 cells to low-dose DTX increased vimentin content (Fig. 5d). In addition, a decrease in actin levels for T24 cells is observed after 72 hours of DTX-treatment (Fig. 5d). In the case of 5637 cells, WB data revealed a slight decrease in actin levels with respect to control cells (Fig. 5c).

### 3.4. Morphology of nuclei forced by MTs organization ruled by DTX treatment.

DTX treatment strongly alters the organization and compaction of MTs and causes mitotic arrest. Additionally, Smith and Xu describe a potential non-mitotic mechanism of paclitaxel action. They show that paclitaxel-induced rigid microtubules can act to break malleable cancer nuclei into multiple micronuclei (Smith and Xu, 2021). Therefore, changes in nuclear morphology are expected as a result of DTX treatment, while standard analysis of the mean projected nucleus area (data not shown) revealed no changes in nuclei morphology after cell exposure to DTX. Then, we used the NII approach to visualize changes in nucleus morphology. Figure S2 shows the morphological analysis of nuclei from 5637 cells treated with low-dose

DTX. For control cells, at each time point, approximately 90% or more of the population have normal nuclei (Fig. S2 a,b,c and Tab. 3). After DTX treatment, we observed a significant increase in the population of irregular (I) nuclei. In addition, large regular and irregular as well as small and small regular nuclei appear or increase in number, while the population of normal nuclei decreases to about 50% after 72 hours of drug treatment. After 24 hours of exposure of 5637 cells to DTX, we already find a slight increase of subpopulations of cells within SR and I nuclei types. While the population of irregular nuclei in control cells was about 4.6% (Tab. 3), it increased to about 7.6% in DTX-treated 5637 cells. The SR nucleus population increased from 3.5% ± 2.2% to 9.4% ± 4.3% after 24 hours of DTX exposure (Fig. S2 a, Tab. 3). After the next 24 hours of drug exposure, the pronounced change in the size of the populations of SR, LR, LI, and I was registered. The LR and I groups accounted for approximately 19% of the total nuclei population. The population of large regular nuclei increased from about 1.3% to 4.6% (Fig. S2 b, Tab. 3). The most spectacular change in the ratio of different types of nuclei shapes was observed in 5637 cells after 72 hours of drug treatment. The population of small regular nuclei increased almost 2-fold when compared to the control group. The number of LR nuclei changed slightly (7.1% ± 2.1% and 4.1% ± 0.4%, respectively). The number of irregularly shaped nuclei also increased in DTX-treated (72 hours) 5637 cells. The most striking change was observed in the size of the large irregular nucleus population. The LI group accounted for approximately 23% of the total number of nuclei examined in 5637 DTX-treated cells.

In the case of T24 cells, DTX treatment caused less spectacular changes in the percentages of different types of nuclear subpopulations (Fig. S3, Tab. 4). Inspection of Figure S3 and Table 4 shows that the most pronounced change occurs in the case of irregularly shaped nuclei. After 24 hours of DTX exposure, the subpopulation of I nuclei represents approximately 8% of the total nuclear population. At 48 and 72 hours of drug treatment, the size of the subpopulation of I nuclei increases to approximately 11% (Fig. S3 b,c, Tab.4). Approximately 10% of T24 cells treated with DTX for 72 hours have small regular and large regular nuclei (4.5% ± 1.1% and 5.4% ± 3.4%, respectively), whereas in control samples these subpopulations were not detected or were small (Tab.4).

Table 3 Proportions of different shapes and sizes of nuclear subpopulations in control and DTX-treated 5637 cells. Data are presented as mean ± SD of the percentage of the total nuclear

population. Groups designated as N-normal, S-small, SR-small regular, SI-small irregular, LR-large regular, LI-large irregular, and I-irregular.

| Percent of nuclei (mean ± SD) | | | | | | |
|---|---|---|---|---|---|---|
| **5637** | **0 + 24 h** | | **0 + 48 h** | | **0 + 72 h** | |
| | **ctr** | **+DTX** | **ctr** | **+DTX** | **ctr** | **+DTX** |
| **N** | 89.6 ± 2.4 | 74.2 ± 8.0 | 94.2 ± 1.2 | 62.9 ± 3.4 | 88 ± 27 | 48 ± 14 |
| **S** | 0.3 ± 0.6 | 4.8 ± 3.0 | 0.2 ± 0.4 | 3.1 ± 0.5 | 0.4 ± 0.6 | 7.9 ± 3.0 |
| **SR** | 3.5 ± 2.2 | 9.4 ± 4.3 | 1.2 ± 1.0 | 9.7 ± 3.4 | 15.9 ± 3.7 | 38 ± 11 |
| **SI** | - | 0.3 ± 0.6 | - | 0.3 ± 0.6 | - | - |
| **LR** | 1.3 ± 1.2 | 2.9 ± 2.1 | 1.3 ± 0.8 | 4.6 ± 1.5 | 4.1 ± 0.4 | 7.1 ± 2.1 |
| **LI** | 1.5 ± 0.5 | 0.7 ± 0.9 | - | 7.2 ± 3.7 | 1.4 ± 1.0 | 23.5 ± 6.9 |
| **I** | 4.6 ± 2.5 | 7.6 ± 1.5 | 3.1 ± 0.7 | 12.2 ± 3.0 | 18.9 ± 9.0 | 25.9 ± 7.6 |

Table ~~2~~ Percentages of different shapes and sizes of nuclear subpopulations in control and DTX-treated T24 cells. Data are presented as mean ± SD. Groups designated as N-normal, S-small, SR-small regular, SI-small irregular, LR-large regular, LI-large irregular, and I-irregular.

| Percent of nuclei (mean ± SD) | | | | | | |
|---|---|---|---|---|---|---|
| **T24** | **0 + 24 h** | | **0 + 48 h** | | **0 + 72 h** | |
| | **ctr** | **+DTX** | **ctr** | **+DTX** | **ctr** | **+DTX** |
| **N** | 98.9 ± 1.6 | 88.7 ± 3.5 | 94.8 ± 5.2 | 81 ± 12 | 98.0 ± 1.0 | 77.3 ± 5.7 |
| **S** | - | 1.7 ± 2.4 | - | 1.1 ± 1.6 | - | - |
| **SR** | - | 1.5 ± 2.1 | - | 1.6 ± 2.2 | - | 4.5 ± 1.1 |
| **SI** | - | - | - | - | - | - |
| **LR** | - | - | 5.2 ± 5.2 | 3.9 ± 2.8 | 1.7 ± 0.5 | 5.4 ± 3.4 |
| **LI** | - | - | - | 1.9 ± 0.6 | - | 1.7 ± 0.5 |
| **I** | - | 8.1 ± 3.2 | - | 10.7 ± 8.0 | 0.3 ± 0.6 | 11.1 ± 5.5 |

### 3.5. Docetaxel reduces the migration of 5637 cells and induces T24 cells to migrate.

Low-dose DTX treatment alters the migration patterns of bladder cancer cells. The data show that 5637 cells are actively migrating even after 96 hours (0+72 h) of culture (Fig. 6 a,c), whereas T24 cells showed reduced migratory ability. Figure 6 (b, d) plots the relationship between displacement and total trajectory length of individual 5637 and T24 cells. In the case of control samples, we observe that among 5637 cells cultured for 72 and 96 hours, there is a subpopulation of cells migrating to distances greater than 75 µm, while under similar conditions, T24 cells migrate to a maximum displacement of less than 50 µm. After the exposure of cells to DTX, the overall migratory potential of 5637 and T24 cells is reduced compared to the control (statistical significance at $p = 0.0001$), however, among T24 cells, we have a group of cells (~10%) that moved a minimum distance of 100 µm (Fig. 6 b,d).

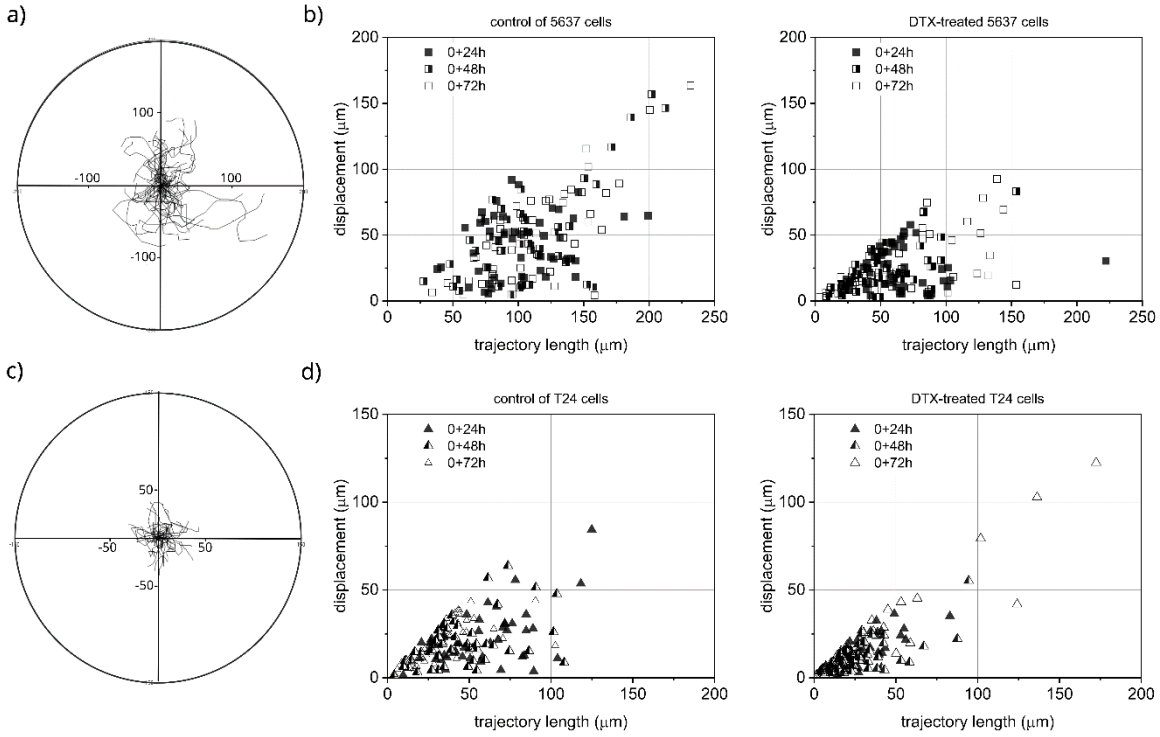


Figure 6 Migration of control and DTX-treated (24, 48, and 72 hours) 5637 and T24 cells (recorded for 8 and 4 hours, respectively, at 10-minute time intervals). In a) and c) exemplary data, trajectories of control 5637 and T24 cells (0 + 72 hours), respectively, are shown as circular plots (axis scale in µm) drawn with the starting point of each trajectory placed at the origin of the graph. The radii of the plots are 200 µm and 150 µm for 5637 and T24 cells, respectively. In b) and d), displacements and total trajectory lengths of control and DTX-treated (24, 48, and 72 hours) 5637 and T24 cells, respectively. Solid symbols refer to 24 hours of DTX treatment, half-open, and open to 48 and 72 hours, respectively.

## 4. Discussion

Our results show that exposure of bladder cancer cells to even a low dose of DTX directly or indirectly induces changes in their structure (shape of nuclei), morphology (height), function (migration, division), and rheology (apparent Young's modulus and shear elastic plateau modulus). AFM-based investigation of T24 and 5637 cells revealed a different response of the cells to DTX treatment. Both nanomechanical and rheological measurements of 5637 cells showed that cell stiffening (positive values of $\Delta E_{rel}$ and $\Delta G_0^{rel}$) increased with longer DTX exposure times. On the other hand, T24 cells were characterized by negative values of $\Delta E_{rel}$ and $\Delta G_0^{rel}$ after 24 and 48 hours of DTX treatment, while after 72 hours, they showed statistically significant but slight stiffening compared to control cells. We did not observe any changes in transition frequency, implying that the internal response of the cytoskeleton to deformations did not differ. An opposite behavior was observed in 5637 cells. After 72 hours of DTX exposure, the range of frequencies where cells exhibited elastic behavior ($G' > G''$) was broader ($f_T^{ctl}$ = 57Hz and $f_T^{DTX}$ = 132 Hz); however, an additional change in the value of the power exponent of $G'$ (a) in the high-frequency range ($f > f_T$) increased from 0.065 ± 0.016 to 0.13 ± 0.03 suggesting a slightly more fluid state of the DTX-treated 5637 than control 5637 cells (possibly more breaks in the cytoskeletal biopolymer networks).

Based on this contrasting behavior, we hypothesized that the mechanism of changes induced by microtubule-targeting agents must depend on the cytoskeleton composition. Therefore, we compared these cell lines by examining their structure and morphology after DTX treatment. We analyzed changes in cell nucleus size and shape using the NII approach, as well as cytoskeletal network organization and protein content using immunostaining and Western blot. NII analysis revealed that for 5637 cells, the subpopulation of normal nuclei (size and shape) decreases to 48 ± 14 % (DTX-treated, 72h). Among the rest, large irregular (LI) and irregular (I) nuclei are dominant subpopulations. These data correlate with changes in the height (increase) of DTX-treated 5637 cells. While the cell height increases, the cell projected area of DTX-treated 5637 cells decreases after 24 hours of exposure, and no statistically significant change in $S$ was found after 48 and 72 hours ($\Delta S_{rel}$ = 7.9 ± 9.6 % and 14 ± 14 %, respectively). In addition, confocal images clearly show an increased concentration of microtubules near the nucleus, which form dense rings that compress the nucleus, resulting in an increase in height rather than the projected cell area and partially irregular shape of nuclei. In the case of T24 cells, the subpopulation of abnormal nuclei is at the level of 20-25%, and the subpopulation of irregular nuclei after 48 hours and longer of DTX treatment is about 10%. Interestingly, after

24 hours of drug exposure, T24 cells increase in height, but $\Delta S_{rel} < 0$. After 72 hours, the height and $S$ of control and treated T24 cells do not differ, accompanied by $\Delta E_{rel} > 0$ (stiffening). The results show no correlation between mechanical properties and cell height. Confocal images of microtubule organization in DTX-treated (72h) T24 cells showed that instead of radial dispersion of MTs, the network is denser and polarized along the cell body of the cells.

This observation correlates with the increased migratory properties of a subpopulation of T24 cells cultured under these conditions. On the other hand, 5637 cells become less migratory after DTX treatment, which is understandable considering the unique organization of MTs, densely packed and grummets, in 5637 cells cultured in a medium containing a low dose of DTX. Close inspection of the confocal images also shows that a rearrangement of the actin network occurs after DTX treatment. While in the case of 5637 cells, there is little or no pronounced change in the intensity of actin filaments (in agreement with WB data), in T24 cells, we observe a significant decrease in the fluorescence intensity of the Alexa 488 label after DTX treatment (in agreement with WB), which is an indicator of a significant deficit of actin when compared to the reference cells. In conclusion, after DTX treatment, we have a denser MTs network and a poorer actin network in T24 cells. Such a cytoskeletal composition is also found in 5637 cells and is accompanied by a pronounced cell stiffening, while T24 cells soften (24 and 48 hours of drug treatment) or slightly stiffen (72 hours). This striking difference suggests that a third factor can adjust the mechanical response of DTX-treated T24 cells. In addition to MTs and actin filaments, a third cytoskeletal component is the vimentin interfilament network, and we hypothesized that both actin and VIFs are responsible for the weak response of DTX-treated T24 to imposed deformation (small perturbations in $E$ and shear plateau modulus, and no changes in transition frequency). It has been reported that vimentin-deficient cells exhibit a less robust microtubule network orientation and greater microtubule fluctuations, as they show impaired migration, contractility, and resistance to mechanical stress (Schaedel et al., 2021), which is exactly the case for 5637 cells and the opposite of T24 cells.

Indeed, after DTX treatment, the vimentin content decreased of about 20% ($0.81 \pm 0.02$, at 72h) in 5637 cells, while in T24 cells, vimentin became more abundant with exposure time ($1.136 \pm 0.083$, $1.129 \pm 0.038$, $1.323 \pm 0.037$ for 24, 48, and 72 hour of DTX treatment, respectively). It explains small subpopulations of irregular nuclei. Vimentin has been shown to regulate nuclear shape and volume and to protect the nucleus from DNA damage (Strouhalova et al., 2020). It also explains very weak changes in rheological properties, as vimentin is known to act as an intracellular shock absorber against tensile stress, being able to efficiently dissipate large

amounts of mechanical energy, thereby protecting cell integrity (Block et al., 2018; Kraxner et al., 2021; Patteson et al., 2020; Schepers et al., 2021; Wu et al., 2022). Wu et al. (Wu et al., 2022) reported that vimentin also contributes to the stiffness of mouse embryonic fibroblasts. Furthermore, increased migratory behavior of vimentin-rich cells has been reported (Battaglia et al., 2018; Kraxner and Köster, 2023; Shaebani et al., 2022; Wu et al., 2022), which is also consistent with our findings. However, another question arises here. DTX-treated T24 cells are rich in microtubules and vimentin, while there is a decrease in actin content (by about 14%, 11%, and 25% for 24h, 48h, and 72h of DTX treatment of T24 cells, respectively). This result indicates that T24 cells soften after 24 and 48 hours of DTX treatment due to a decrease in actin levels, which cannot be compensated by an increase in vimentin, as both are at similar levels. However, after 72 hours, an increase in vimentin levels is pronounced compared to the decrease in actin content. Nevertheless, it is intriguing why we do not observe a more pronounced stiffening of the cells (72 hours of drug exposure). The explanation may be related to the fact that taxanes induce phosphorylation of vimentin (Kroning and Lichtenstein, 1998; Kuburich et al., 2023; Strouhalova et al., 2020; Vilalta et al., 1998). The N-terminus of vimentin has a large negative charge, targeted by several protein kinases that phosphorylate neutral serine residues, inducing further charge changes (Patteson et al., 2021). These can lead to filament disassembly, reducing the stiffness of the VIF network (Kraxner et al., 2021; Patteson et al., 2021). Thus, we conclude that in the case of T24 cells, we do not observe alterations in rheological properties after DTX treatment due to the crosstalk of microtubule, actin, and vimentin networks. Reorganization and higher density of MTs is accompanied by a decrease of actin and a simultaneous increase of vimentin, shock absorber, but due to partial disassembly of the VIF network, we do not observe stiffening of DTX-treated T24 cells. In the case of 5637, our data indicate that no pronounced changes in actin and VIFs content occur after treatment, and thus, the density and arrangement of the MTs network determine the mechanical properties of 5637 cells as well as their resistance to mechanical stress.

## 5. Conclusion

Here, we report that the balance between three major cytoskeletal networks regulates the stress resistance of DTX-treated T24 cells. Our data show the relevance of the VIFs network in preserving the mechanical properties of T24 after exposure to a microtubule targeting agent cannot be excluded. This new finding will undoubtedly open up new avenues for a broader study of the function of VIFs, which have often been assumed to be of minor relevance to cell mechanics due to their short persistence length compared to MFs and MTs. We also report that

compensation by one of the components for changes induced in other cytoskeletal components is cell-dependent. Due to the complexity of the cytoskeleton network, further studies are needed to understand the role of intermittent filaments in cell rheology fully. We also revealed that within DTX-treated T24 cells, there is a subpopulation of cells with increased migratory potential. The presented results suggest that this is worthy of further investigation as DTX is used in BC second-line therapies.

## Acknowledgments

Joanna Zemła acknowledges the financial support of the French Government and the French Embassy in Poland. Claude Verdier is a member of LabeX Tec21 (Invest. D'Avenir: grant No. ANR_11_LABX_0030).

## Supplementary materials

DTX cytotoxicity tests- MTS assay results; Figures showing variations of the Nucleus Irregularity Index (NII) of T24 and 5637 cells treated with DTX (24h, 48h, and 72h); Displacement distributions of control and DTX treated 5637 and T24 cells. An exemple of the Western Blot gel. Brief introduction of the power-law rheology for cells.

## References

Abidine, Y., Constantinescu, A., Laurent, V.M., Sundar Rajan, V., Michel, R., Laplaud, V., Duperray, A., Verdier, C., 2018. Mechanosensitivity of Cancer Cells in Contact with Soft Substrates Using AFM. Biophys J 114, 1165–1175. https://doi.org/10.1016/j.bpj.2018.01.005

Abidine, Y., Giannetti, A., Revilloud, J., Laurent, V.M., Verdier, C., 2021. Viscoelastic properties in cancer: From cells to spheroids. Cells 10, 1704. https://doi.org/10.3390/cells10071704

Abidine, Y., Laurent, V.M., Michel, R., Duperray, A., Palade, L.I., Verdier, C., 2015. Physical properties of polyacrylamide gels probed by AFM and rheology. EPL 109, 38003. https://doi.org/10.1209/0295-5075/109/38003

Alcaraz, J., Buscemi, L., Grabulosa, M., Trepat, X., Fabry, B., Farré, R., Navajas, D., 2003. Microrheology of human lung epithelial cells measured by atomic force microscopy. Biophys J 84, 2071–2079. https://doi.org/10.1016/S0006-3495(03)75014-0

Antoni, S., Ferlay, J., Soerjomataram, I., Znaor, A., Jemal, A., Bray, F., 2017. Bladder Cancer Incidence and Mortality: A Global Overview and Recent Trends. Eur Urol 71, 96–108. https://doi.org/10.1016/j.eururo.2016.06.010

Battaglia, R.A., Delic, S., Herrmann, H., Snider, N.T., 2018. Vimentin on the move: New developments in cell migration. F1000Res. https://doi.org/10.12688/f1000research.15967.1

620 Block, J., Witt, H., Candelli, A., Cabanas Danes, J., G Peterman, E.J., L Wuite, G.J., Janshoff, A., Köster,
621 S., 2018. Viscoelastic properties of vimentin originate from nonequilibrium conformational
622 changes. Sci Adv 4, eaat1161. https://doi.org/10.1126/sciadv.aat1161

623 Bobrowska, J., Pabijan, J., Wiltowska-Zuber, J., Jany, B.R., Krok, F., Awsiuk, K., Rysz, J., Budkowski, A.,
624 Lekka, M., 2016. Data on step-by-step atomic force microscopy monitoring of changes occurring
625 in single melanoma cells undergoing ToF SIMS specialized sample preparation protocol. Data
626 Brief 8, 1322–1332. https://doi.org/10.1016/j.dib.2016.07.052

627 Čermák, V., Dostál, V., Jelínek, M., Libusová, L., Kovář, J., Rösel, D., Brábek, J., 2020. Microtubule-
628 targeting agents and their impact on cancer treatment. Eur J Cell Biol., 151075.
629 https://doi.org/10.1016/j.ejcb.2020.151075

630 Derely, L., Collart Dutilleul, P.-Y., Michotte de Welle, S., Szabo, V., Gergely, C., Cuisinier, F.J.G., 2011.
631 Raman confocal microscopy and AFM combined studies of cancerous cells treated with
632 Paclitaxel, in: Nanoscale Imaging, Sensing, and Actuation for Biomedical Applications VIII. SPIE,
633 79080H. https://doi.org/10.1117/12.874893

634 El Kaffas, A., Bekah, D., Rui, M., Carl Kumaradas, J., Kolios, M.C., 2013. Investigating longitudinal
635 changes in the mechanical properties of MCF-7 cells exposed to paclitaxol using particle
636 tracking microrheology. Phys Med Biol 58, 923–936. https://doi.org/10.1088/0031-
637 9155/58/4/923

638 Filippi-Chiela, E.C., Oliveira, M.M., Jurkovski, B., Sm, C.-J., Vdd, S., 2012. Nuclear Morphometric
639 Analysis (NMA): Screening of Senescence, Apoptosis and Nuclear Irregularities. PLoS One 7,
640 42522. https://doi.org/10.1371/journal.pone.0042522

641 Flormann, D.A.D., Anton, C., Pohland, M.O., Bautz, Y., Kaub, K., Terriac, E., Schäffer, T.E.,
642 Rheinlaender, J., Janshoff, A., Ott, A., Lautenschläger, F., 2021. Oscillatory Microrheology, Creep
643 Compliance and Stress Relaxation of Biological Cells Reveal Strong Correlations as Probed by
644 Atomic Force Microscopy. Front Phys 9, 1–12. https://doi.org/10.3389/fphy.2021.711860

645 Fojo, T., Menefee, M., 2007. Mechanisms of multidrug resistance: The potential role of microtubule-
646 stabilizing agents. Annals of Oncology 18, v3–v8. https://doi.org/10.1093/annonc/mdm172

647 Hecht, F.M., Rheinlaender, J., Schierbaum, N., Goldmann, W.H., Fabry, B., Schäffer, T.E., 2015.
648 Imaging viscoelastic properties of live cells by AFM: Power-law rheology on the nanoscale. Soft
649 Matter 11, 4584–4591. https://doi.org/10.1039/c4sm02718c

650 Hosseini, K., Frenzel, A., Fischer-Friedrich, E., 2021. EMT changes actin cortex rheology in a cell-cycle-
651 dependent manner. Biophys J 120, 3516–3526. https://doi.org/10.1016/j.bpj.2021.05.006

652 Hosseini, K., Trus, P., Frenzel, A., Werner, C., Fischer-Friedrich, E., 2022. Skin epithelial cells change
653 their mechanics and proliferation upon snail-mediated EMT signalling. Soft Matter 18, 2585–
654 2596. https://doi.org/10.1039/d2sm00159d

655 Hou, Y., Zhao, C., Xu, B., Huang, Y., Liu, C., 2021. Effect of docetaxel on mechanical properties of
656 ovarian cancer cells. Exp Cell Res 408, 112853. https://doi.org/10.1016/j.yexcr.2021.112853

657 Hung, M.S., Tsai, M.F., 2015. Investigating the Influence of Anti-Cancer Drugs on the Mechanics of
658 Cells Using AFM. Bionanoscience 5, 156–161. https://doi.org/10.1007/s12668-015-0174-9

659 Korohoda, W., Madeja, Z., 1997. Contact of sarcoma cells with aligned fibroblasts accelerates their
660 displacement: Computer-assisted analysis of tumour cell locomotion in co-culture. Biochemistry
661 and Cell Biology 75, 263–276. https://doi.org/10.1139/o97-049

662 Kraxner, J., Köster, S., 2023. Influence of phosphorylation on intermediate filaments. Biol Chem. 404,
663 821-827. https://doi.org/10.1515/hsz-2023-0140

664 Kraxner, J., Lorenz, C., Menzel, J., Parfentev, I., Silbern, I., Denz, M., Urlaub, H., Schwappach, B.,
665 Köster, S., 2021. Post-translational modifications soften vimentin intermediate filaments †.
666 Nanoscale 13, 380–387. https://doi.org/10.1039/d0nr07322a

667 Kroning, R., Lichtenstein, A., 1998. Taxol can induce phosphorylation of BCL-2 in multiple myeloma
668 cells and potentiate dexamethasone-induced apoptosis. Pergamon Lmkemia Research 22, 275-
669 286. https://doi.org/10.1016/S0145-2126(97)00170-7

670 Kubiak, A., Chighizola, M., Schulte, C., Bryniarska, N., Wesolowska, J., Pudelek, M., Lasota, M.,
671 Ryszawy, D., Basta-Kaim, A., Laidler, P., Podestà, A., Lekka, M., 2021. Stiffening of DU145
672 prostate cancer cells driven by actin filaments-microtubule crosstalk conferring resistance to
673 microtubule-targeting drugs. Nanoscale 13, 6212–6226. https://doi.org/10.1039/d0nr06464e

674 Kubiak, A., Zieliński, T., Pabijan, J., Lekka, M., 2020. Nanomechanics in monitoring the effectiveness
675 of drugs targeting the cancer cell cytoskeleton. Int J Mol Sci. 22, 1-15.
676 https://doi.org/10.3390/ijms21228786

677 Kuburich, N.A., den Hollander, P., Castaneda, M., Pietilä, M., Tang, X., Batra, H., Martínez-Peña, F.,
678 Visal, T.H., Zhou, T., Demestichas, B.R., Dontula, R. V., Liu, J.Y., Maddela, J.J., Padmanabhan,
679 R.S., Phi, L.T.H., Rosolen, M.J., Sabapathy, T., Kumar, D., Giancotti, F.G., Lairson, L.L., Raso, M.G.,
680 Soundararajan, R., Mani, S.A., 2023. Stabilizing vimentin phosphorylation inhibits stem-like cell
681 properties and metastasis of hybrid epithelial/mesenchymal carcinomas. Cell Rep 42., 113470.
682 https://doi.org/10.1016/j.celrep.2023.113470

683 Lekka, M., Lekki, J., Marszałek, M., Golonka, P., Stachura, Z., Cleff, B., Hrynkiewicz, A.Z., 1999. Local
684 elastic properties of cells studied by SFM. Appl Surf Sci 141, 345–349.
685 https://doi.org/10.1016/S0169-4332(98)00522-4

686 Luty, M., Szydlak, R., Pabijan, J., Øvreeide, I.H., Prot, V.E., Zemła, J., Stokke, B.T., Lekka, M., 2023.
687 Migration, proliferation, and elasticity of bladder cancer cells on lectin-coated surfaces. bioRxiv
688 15. https://doi.org/10.1101/2024.05.12.593008

689 Michalakis, J., Georgatos, S.D., Romanos, J., Koutala, H., Georgoulias, V., Tsiftsis, D., Theodoropoulos,
690 P.A., 2005. Micromolar taxol, with or without hyperthermia, induces mitotic catastrophe and
691 cell necrosis in HeLa cells. Cancer Chemother Pharmacol 56, 615–622.
692 https://doi.org/10.1007/s00280-005-1002-7

693 Morse, D.L., Gray, H., Payne, C.M., Gillies, R.J., 2005. Docetaxel induces cell death through mitotic
694 catastrophe in human breast cancer cells. Mol Cancer Ther 4, 1495–1504.
695 https://doi.org/10.1158/1535-7163.MCT-05-0130

696 Patel, S.H., Gabrielson, A., Collins, C., Singla, N., Bivalacqua, T., Hahn, N.M., Kates, M.R., Buchanan
697 Brady, J., 2023. 507 Poster Session Intravesical gemcitabine and docetaxel in the treatment of
698 BCG-nä ıve non-muscle in-vasive urothelial carcinoma of the bladder: Updates from a phase 2
699 trial.

Patteson, A.E., Carroll, R.J., Iwamoto, D. V, Janmey, P.A., 2021. The vimentin cytoskeleton: when polymer physics meets cell biology. Phys. Biol 18, 11001. https://doi.org/10.1088/1478-3975/abbcc2

Prauzner-Bechcicki, S., Raczkowska, J., Madej, E., Pabijan, J., Lukes, J., Sepitka, J., Rysz, J., Awsiuk, K., Bernasik, A., Budkowski, A., Lekka, M., 2015. PDMS substrate stiffness affects the morphology and growth profiles of cancerous prostate and melanoma cells. J Mech Behav Biomed Mater 41. https://doi.org/10.1016/j.jmbbm.2014.09.020

Ramos, J.R., Pabijan, J., Garcia, R., Lekka, M., 2014. The softening of human bladder cancer cells happens at an early stage of the malignancy process. Beilstein Journal of Nanotechnology 5, 447–457. https://doi.org/10.3762/bjnano.5.52

Ren, J., Huang, H., Liu, Y., Zheng, X., Zou, Q., 2015. An atomic force microscope study revealed two mechanisms in the effect of anticancer drugs on rate-dependent Young's modulus of human prostate cancer cells. PLoS One 10, e0126107. https://doi.org/10.1371/journal.pone.0126107

Roumiguié, M., Black, P.C., 2022. Sequential Gemcitabine plus Docetaxel Is the Standard Second-line Intravesical Therapy for BCG-unresponsive Non–muscle-invasive bladder cancer: Pro. Eur Urol Focus 4, 1117-1120. https://doi.org/10.1016/j.euf.2021.07.018

Sader, J.E., Chon, J.W.M., Mulvaney, P., 1999. Calibration of rectangular atomic force microscope cantilevers. Review of Scientific Instruments 70, 3967–3969. https://doi.org/10.1063/1.1150021

Sanli, O., Dobruch, J., Knowles, M.A., Burger, M., Alemozaffar, M., Nielsen, M.E., Lotan, Y., 2017. Bladder cancer. Nat Rev Dis Primers 3, 1–19. https://doi.org/10.1038/nrdp.2017.22

Schaedel, L., Lorenz, C., Schepers, A. V, Klumpp, S., Köster, S., 2021. Vimentin intermediate filaments stabilize dynamic microtubules by direct interactions. Nat Commun 12, 3799. https://doi.org/10.1038/s41467-021-23523-z

Schepers, A. V, Lorenz, C., Nietmann, P., Janshoff, A., Klumpp, S., 2021. Multiscale mechanics and temporal evolution of vimentin intermediate filament networks. PNAS 118, e2102026118. https://doi.org/10.1073/pnas.2102026118/-/DCSupplemental.y

Schillers, H., Rianna, C., Schäpe, J., Luque, T., Doschke, H., Wälte, M., Uriarte, J.J., Campillo, N., Michanetzis, G.P.A., Bobrowska, J., Dumitru, A., Herruzo, E.T., Bovio, S., Parot, P., Galluzzi, M., Podestà, A., Puricelli, L., Scheuring, S., Missirlis, Y., Garcia, R., Odorico, M., Teulon, J.M., Lafont, F., Lekka, M., Rico, F., Rigato, A., Pellequer, J.L., Oberleithner, H., Navajas, D., Radmacher, M., 2017. Standardized Nanomechanical Atomic Force Microscopy Procedure (SNAP) for Measuring Soft and Biological Samples. Sci Rep 7, 5117. https://doi.org/10.1038/s41598-017-05383-0

Shaebani, M.R., Stankevicins, L., Vesperini, D., Urbanska, M., Flormann, D.A.D., Terriac, E., Gad, A.K.B., Cheng, F., Eriksson, J.E., Lautenschläger, F., 2022. Effects of vimentin on the migration, search efficiency, and mechanical resilience of dendritic cells. Biophys J 121, 3950–3961. https://doi.org/10.1016/j.bpj.2022.08.033

Škubník, J., Pavlíčková, V., Ruml, T., Rimpelová, S., 2021. Current perspectives on taxanes: Focus on their bioactivity, delivery and combination therapy. Plants 3, 569. https://doi.org/10.3390/plants10030569

Smith, E.R., Xu, X.-X., 2021. Breaking malignant nuclei as a non-mitotic mechanism of taxol-paclitaxel. J Cancer Biol 2, 86–93. https://doi.org/10.46439/cancerbiology.2.031

Strouhalova, K., Přechová, M., Gandalovičová, A., Brábek, J., Gregor, M., Rosel, D., 2020. Vimentin Intermediate Filaments as Potential Target for Cancer Treatment. Cancers (Basel) 12, 184. https://doi.org/10.3390/cancers12010184

Tang, N.T., Robinson, R., Snook, R.D., Brown, M., Clarke, N., Gardner, P., 2023. Classification of formalin-fixed bladder cancer cells with laser tweezer Raman spectroscopy. Analyst 148, 4099–4108. https://doi.org/10.1039/d3an00119a

Vilalta, P.M., Zhang Liping, Hamm-Alvarez, S.F., 1998. A novel taxol-induced vimentin phosphorylation and stabilization revealed by studies on stable microtubules and vimentin intermediate filaments. J Cell Sci 111, 1841–1852. https://doi.org/10.1242/jcs.111.13.1841

Wu, H., Shen, Y., Sivagurunathan, S., Weber, M.S., Adam, S.A., Shin, J.H., Fredberg, J.J., Medalia, O., Goldman, R., Weitz, D.A., Lippincott-Schwartz, J., 2022. Vimentin intermediate filaments and filamentous actin form unexpected interpenetrating networks that redefine the cell cortex. PNAS 119, e2115217119. https://doi.org/10.1073/pnas.2115217119/-/DCSupplemental

Zemła, J., Bobrowska, J., Kubiak, A., Zieliński, T., Pabijan, J., Pogoda, K., Bobrowski, P., Lekka, M., 2020. Indenting soft samples (hydrogels and cells) with cantilevers possessing various shapes of probing tip. European Biophysics Journal 49, 485–495. https://doi.org/10.1007/s00249-020-01456-7

**Authors Contributions**: Conceptualization, J.Z., M.L.; Investigation, J.Z., M.Lu., J.P.; Formal analysis, J.Z., C.V., M.Lu.; Visualization, J.Z., C.V.; Writing- original draft, J.Z.; Funding acquisition, J.Z., C.V.; Resources, M.L., C.V.; Writing- review and editing, M.L., C.V.; All authors have read and agreed to the published version of the manuscript.

**Data Availability Statement**: Data is available from the authors upon request.

**Conflicts of Interest**: "The authors declare no conflict of interest."

Joanna Zemła: joanna.zemla@ifj.edu.pl; ORCID: 0000-0003-0980-4649

Claude Verdier: claude.verdier@univ-grenoble-alpes.fr; ORCID: 0000-0003-3706-7148

Marcin Luty: marcin.luty@ifj.edu.pl; ORCID: 0000-0002-8332-8962

Joanna Pabijan: joanna.pabijan@ifj.edu.pl, ORCID: 0000-0003-4518-1389

Małgorzata Lekka: malgorzata.lekka@ifj.edu.pl, ORCID: 0000-0003-0844-8662